
IDP-PGFE: An Interpretable Disruption Predictor based on Physics-Guided Feature Extraction

Chengshuo Shen, Wei Zheng*, Yonghua Ding, Xinkun Ai, Fengming Xue, Yu Zhong, Nengchao Wang, Li Gao, Zhipeng Chen, Zhoujun Yang, Zhongyong Chen, Yuan Pan and J-TEXT team[†]

International Joint Research Laboratory of Magnetic Confinement Fusion and Plasma Physics, State Key Laboratory of Advanced Electromagnetic Engineering and Technology, School of Electrical and Electronic Engineering, Huazhong University of Science and Technology, Wuhan, 430074, China

Email:

shenchengshuo@hust.edu.cn, zhengwei@hust.edu.cn

Abstract

Disruption prediction has made rapid progress in recent years, especially machine learning (ML)-based methods. Understanding why a predictor makes a certain prediction can be as crucial as the prediction's accuracy for future tokamak disruption predictors. The purpose of most disruption predictors is accuracy or cross-machine capability. However, if a disruption prediction model can be interpreted, it can tell why certain samples are classified as disruption precursors. This allows us to tell the types of incoming disruption and gives us insight into the mechanism of disruption. This paper design a disruption predictor called Interpretable Disruption Predictor based On Physics-guided feature extraction (IDP-PGFE) on J-TEXT. The prediction performance of model is effectively improved (TPR = 97.27%, FPR = 5.45%, AUC = 0.98) by extracting physics-guided features. A high-performance model is required to ensure the validity of the interpretation results. The interpretability study of IDP-PGFE provides an understanding of J-TEXT disruption and is generally consistent with existing comprehension of disruption. IDP-PGFE has been applied to the disruption due to continuously increasing density towards density limit experiments on J-TEXT. The time evolution of the PGFE features contribution demonstrates that the application of ECRH triggers radiation-caused disruption, which lowers the density at disruption. While the application of RMP indeed raises the density limit in J-TEXT. The interpretability study guides intuition on the physical mechanisms of density limit disruption that RMPs affect not only the MHD instabilities but also the radiation profile, which delays density limit disruption. Physics-guided feature extraction could also reduce the data requirement of IDP-PGFE to 10% of the data needed by the model that uses raw data as input. Therefore, IDP-PGFE is an efficient approach to interpreting data-driven disruption prediction models for further disruption mechanisms and transfer research.

Keywords: interpretability, disruption prediction, machine learning, feature extraction

[†] SEE THE AUTHOR LIST OF "N. WANG *ET AL* 2022 ADVANCES IN PHYSICS AND APPLICATIONS OF 3D MAGNETIC PERTURBATIONS ON THE J-TEXT TOKAMAK, *NUCL. FUSION* 62 042016"

1. Introduction

Disruption is a catastrophic event of the tokamak, which is unacceptable in next generation high performance tokamaks, like ITER, DEMO and CFETR^{1,2}. Therefore, the safe and stable operation of next generation tokamaks requires effectively avoiding and mitigating disruption³, which relies on predictions and in-depth understanding of plasma instabilities and disruption.

The complexity of the physical mechanism of disruption leads to the difficulty in using first-principle models to forecast plasma instabilities and disruptions⁴. To date, physics-driven and data-driven are two main approaches to study disruption prediction. On the one hand, physics-driven disruption prediction studies⁵⁻⁷ put effort on identify disruption or instabilities event chains for operators to avoid disruptions. Such as the disruption event characterization and forecasting (DECAF)⁸ suite contains first-principle, physics-based modules for instabilities identification in tokamaks. On the other hand, most disruption predictors in tokamak devices are based on data-driven method because of the better performance and computing speed⁹⁻¹³.

However, most of these data-driven models do not necessarily reflect the dynamics behind the phenomenon. Their physics fidelity and the interpretability of their results require in-depth investigation. The physics-driven models try to combine the advantages of both paradigms by adopting surrogate machine learning (ML) models¹⁴, which could also improve the interpretability of these ML models. In data-driven method studies, an interpretability model, achieved by applying symbolic regression methods¹⁵⁻¹⁷, has been obtained with the support vector machine (SVM) in JET. An approach to interpret the 1.5D convolutional neural network (CNN) model has also been developed in HL-2A¹⁸, which is a counterfactual-based interpretable approach. The physics-based indicators of disruption precursors based on temperature, density, and radiation profiles have been used to interpret machine learning-based disruption predictors across tokamaks on DIII-D and JET¹⁹.

The interpretable disruption prediction research is in the infancy stage. In comparison, the interpretability study has made progress in machine learning research these years. A prototypical part network (ProtoPNet) is a deep interpretable network architecture, which dissects the image by finding prototypical parts and combines evidence from the prototypes to make a final classification²⁰. The perspective that guided the interpretability model design is that we should stop "interpreting" decisions made by black-box models after the fact and instead build models that are constructively interpretable²¹. This kind of perspective could also be suitable for disruption prediction and inspire us that we should design a disruption predictor that is inherently interpretable properties of its own. In mathematics, machine learning-guided intuition helps us to prove theorem via

attribution techniques²². SHapley Additive exPlanations (SHAP) is a unified attribution-based interpretable approach²³⁻²⁵, which has already been successfully applied in explaining the prediction of hypoxaemia during surgery²⁶.

The perspective and techniques in machine learning research could give us more inspiration on the interpretable disruption prediction research. The purpose of most disruption predictors is accuracy or cross-machine capability. In this work, we would like to design a disruption predictor on the purpose of both accuracy and interpretability. In our previous work, SHAP has been applied to the LightGBM²⁷ based disruption predictors for J-TEXT and HL-2A²⁸. The interpretability study provided a strategy for selecting diagnostics and shots data for developing cross-machine predictors. However, the interpretability of the model is not yet in-depth enough due to the limitations of the input signals, the raw diagnostic signals. So that even if the model is interpretable, the analysis or understanding is just making the connection between disruption and diagnostics, which is very hard to come up with patterns with physical meanings. At the same time, the accuracy of the predictor is also not as good as recent disruption predictors because the tree-based model is not as capable of feature extraction as deep learning. Cristina's work found that physics-based disruption markers in data-driven algorithms are a promising path toward the realization of a uniform framework to predict and interpret disruptive scenarios across different tokamaks¹⁹. An interpretable disruption predictor could also be designed based on physics-based disruption markers. Therefore, in this work, we would like to design an interpretable disruption predictor based on physics-based disruption markers by using SHAP as the interpretable approach.

The way to obtain the physics-based disruption markers in our work is called Physics-Guided Feature Extraction (PGFE). The aim of PGFE is not only enable the model interpretability but also improve the accuracy of the predictor. Deep learning's powerful feature extraction capabilities make it typically outperform traditional machine learning when using a large enough amount of raw signals. However, when there is not enough data, inductive bias can be informed to the network to better embedded known knowledge of disruption in the model. Inductive bias will limit the search domain of the machine learning algorithm, so it can get a better result when there is not enough data. By using known knowledge of disruption, feature engineering reduced the feature dimension using domain knowledge, thus limiting the search model of the training algorithm so that it can be considered as add inductive bias. Adding domain knowledge to machine learning is thought to be useful when the data is not extremely large²⁹, and it is the base for meaningful physical interpretation. PGFE could even reduce the data requirement of the predictor. Due to the high cost of disruptive data from ITER and next-generation tokamaks, disruption prediction researchers need to

find a way to cross-machine prediction or reduce the requirement of disruptive data. Cross-machine has been studied through deep learning³⁰⁻³² and adaptive learning³³. However, they still require disruption data or a large amount of non-disruption data from the new device to train a mixed data model or transfer. Transformer³⁴ is a model with less inductive bias than CNN or recurrent neural network (RNN), as a result in the great performance in both computer vision (CV) and natural language processing (NLP) tasks. However, the cost of transformer is that more data is required to train the model as bias of this model is very low. Inductive bias in PFGE is more specific to disruption prediction task, therefore, train the model with less data is accessible. It is possible to achieve a disruption prediction model of new device directly using a small amount of discharges data with PGFE.

In this paper, an Interpretable Disruption Predictor based On PGFE (IDP-PGFE) has been introduced. The purpose of this work and the advantages of PGFE has been described in this section already. The next section will describe the structure of IDP-PGFE, which consists of a feature extractor, a disruption classifier and an explainer. Section 3 introduced the dataset of IDP-PGFE. The predictive performance of IDP-PGFE is followed in section 4, which shows the two advantages of PGFE. Section 5 examines in detail the interpretability of the predictor including its application to the J-TEXT physics experiment. Section 6 will give a brief discussion on the potentials and limitations of IDP-PGFE. The summary is in section 7.

2. The three components of IDP-PGFE: feature extractor, disruption classifier and explainer

A disruption predictor consists of two components, feature extractor and disruption classifier. However, it is not enough for an interpretable study of the predictor. Explainer is a necessary additional component for interpretable disruption predictor to support the interpretable study. Therefore, IDP-PGFE consists of three components, feature extractor, disruption classifier and explainer. This section will describe these three components of the IDP-PGFE.

2.1 Feature extractor: PGFE

Deep learning models using CNN or RNN to extract features as the feature extraction layer, then feed the features into a fully connected neural network as the classifier layer. However, the diagnostics signals in tokamak experiment are heterogeneous, meaning not all dimensions share the same physical meaning, and the relation among them are very complex. This makes it very hard to get physically meaningful patterns from the interpretation results. PGFE engineering is "white-box", which extracts features with physical meanings for in-depth study after the explainer.

Multiple physical phenomena that may be part of a chain of disruption⁵ can be observed in tokamaks. In this work, the physics-guided features have been extracted based on MHD instabilities, radiation, density related disruptions and basic plasma control system (PCS) signals. The descriptions of features and diagnostics for extracting them can be found in table 1. The numbers followed the diagnostic in the third column is the number of channels used for feature extraction. MHD instability is a significant precursor to disruption, especially the locked mode⁵. Moreover, 2/1 magnetic island growth³⁵ and multi-magnetic island overlap^{36,37} are also considered to be the possible precursors of disruption. In this work, Mirnov probes and locked mode detectors are used to extract this type of features, as listed in the first row of Table 1. Temperature hollowing and edge cooling³⁸ are two risk indicators for MHD instabilities, and they could also be treated as the disruption precursors. Two radiation arrays, soft x-ray (SXR)³⁹ and Absolute eXtended Ultra Violet (AXUV)⁴⁰ arrays are used to extract this type of features due to the difficulty in accessing temperature profiles in all the discharges in the dataset. Greenwald density limit⁴¹ calculated through the scaling law could be considered as a disruption type that can be predicted by a formula. However, density limit disruption usually does not reach the Greenwald density limit in J-TEXT. Therefore, the scaling law is not suitable for predicting disruptions in J-TEXT density limit disruption, density related precursors could be extracted through far-infrared three-wave polarimeter-interferometer (FIR)⁴². The others are basic PCS signals, where the differential of the horizontal and vertical currents can effectively reflect the plasma control information and is extracted as features. Details of MHD instabilities, radiation and density related features extraction engineering are described followed.

In J-TEXT, the growth of $m/n = 2/1$ tearing mode (TM) and multi-magnetic islands overlap are the possible precursors of disruption. Mirnov probes and locked mode detectors are the fundamental diagnostics for MHD instabilities measurement in J-TEXT⁴³, which provide a simple, robust measurement of static and fluctuating magnetic properties. In the limiter configuration with a circular cross-section of J-TEXT plasma, the features "Mir_abs", "Mir_fre" and "Mir_VV" are extracted through one Mirnov probe; "mode_number_m" (MNM) and "mode_number_n" (MNN) are extracted from two Mirnov probes in poloidal and toroidal array, respectively; and " $n = 1$ amplitude" is extracted from two pairs of locked mode detectors, each pair consists of two locked mode detectors with the toroidal angle of 180°.

"Mir_VV" is the peak-to-peak value of the Mirnov probe after a low-pass filter with cutoff frequency of 50 kHz. The typical frequency of 2/1 tearing mode in J-TEXT is approximately 3 kHz. A sliding window of 5 ms (longer than 5 periods of TM rotation) is selected as the time window of the Fast Fourier Transform (FFT) on the Mirnov probe. $X(f)$

represents the Fourier transform of the i^{th} time window (slice). "*Mir_abs*" and "*Mir_fre*" are the intensity and frequency of $X(f)$. If there are multiple frequencies in the Mirnov probe frequency spectrum, the one with the highest spectral intensity will be selected. Here, we did not use the integral Mirnov signals to avoid the zero drift uncertainty between different discharges that contributed to our prediction.

$X_1^i(f)$ and $X_2^i(f)$ could represent the Fourier transform of two Mirnov probe signals of each slice. Their cross spectral density (CSD) can be expressed as

$$P_{12}^i(f) = X_1^{i*}(f)X_2^i(f) = A(f)e^{i\delta_{12}^i(f)} \quad (2-1)$$

where $P_{12}^i(f)$ is the cross spectral density between two Mirnov probes, $A(f)$ is the absolute value of $P_{12}^i(f)$, $\delta_{12}^i(f)$ is the phase of $P_{12}^i(f)$. If the two Mirnov probes are in the poloidal array, the mode number m can be calculated as

$$m = \frac{\delta_{12}^i(f)}{\theta} \quad (2-2)$$

where θ is the poloidal separation between the two Mirnov probes. In J-TEXT, $m = 3$ and $m = 2$ mode often lead to a multi-magnetic island caused disruption. Hence, the mode number is using a weighted average mode number indication, which is described as (2-3)

$$\langle m \rangle = \frac{\sum \delta_{12}^i(f_k)A(f_k)}{\theta \sum A(f_k)} \quad (2-3)$$

where k represents the different frequency of the CSD. MNN is also calculated like this. To increase the accuracy of MNM and MNN , only the frequency component with a coherence larger than 0.95 will be considered.

A typical discharge with tearing mode of J-TEXT is shown in Figure 1. The evolution of MNM , MNN , *Mir_fre*, and *Mir_abs* with the raw Mirnov signals are shown. Because the weighted average mode number indication, MNM and MNN are continuous. The slowdown of mode frequency and growth of mode amplitude induced disruption after the short duration locked mode (less than 1ms). The m/n of this mode are 2/1 and the *Mir_fre* is approximately 3 kHz before mode locking. The ramp down of *Mir_fre* represent the mode locking.

Therefore, after mode locking, $n = 1$ amplitude will be the main MHD-related feature. The magnetic field measured by the LM detector can be expressed as

$$B_r(\theta, \varphi) = \sum b_r^{n=i} \cos(m\theta + n\varphi + \xi^{n=i}) \quad (2-4)$$

where θ and φ is the poloidal and toroidal location of the LM detector, m and n are the poloidal and toroidal mode number, ξ is the spiral phase. If only consider the main component in J-TEXT, which are $n = 0, 1$ and 2 , for the detector on the middle plane $\theta = 0$ (The following are all based on this situation), equation (3-4) can be expressed as

$$B_r(\theta = 0, \varphi) = b_r^{n=0} + b_r^{n=1} \cos(\varphi + \xi^{n=1}) + b_r^{n=2} \cos(2\varphi + \xi^{n=2}) \quad (2-5)$$

$n = 1$ amplitude, $b_r^{n=1}$ can be calculated through two LM detectors with $\Delta\varphi = \pi$, which is shown in equation (6)

$$b_r^{n=1} \cos(\varphi + \xi^{n=1}) = \frac{B_r(\varphi) - B_r(\varphi + \pi)}{2} \quad (2-6)$$

Then $b_r^{n=1}$ and $\xi^{n=1}$ can be calculated by fitting two pairs of these LM detectors. The application of $n = 1$ amplitude on the RMP experiments has been introduced in our review paper on magnetic diagnostics ⁴³.

Table 1 Descriptions and symbols of all the features

Types of features	Relation to disruption	Channels of diagnostics	Symbol
MHD instabilities related	2/1 magnetic island growth; Multi-magnetic island overlaps; Locked mode	Mirnov probe in poloidal array	Mir_abs
			Mir_fre
			Mir_VV
		Mirnov probes in poloidal array (2)	mode_number_m
		Mirnov probes in toroidal array (2)	mode_number_n
Radiation related	Temperature hollowing; Edge cooling;	Locked mode detectors (4)	n=1 amplitude
		AXUV array (30)	P_rad
		SXR_MID	SXR_core
		CIII_MID	CIII
		AXUV array (30)	AXUV_kurt (skew, var)
Density related	Density limit	SXR array (30)	SXR_kurt (skew, var)
		FIR_MID	n _{e0}
		FIR (17)	FIR_kurt (skew, var)
		FIR (17)	sum_n _{e0}
		B _t , I _p	B _t , I _p
Basic PCS signals	Plasma out of control;	I _{hf} , I _{vf}	I _{hf} , I _{vf}
		d _r , d _z	I _{hf_diff} , I _{vf_diff} d _r , d _z

2.1.1 MHD instabilities related features

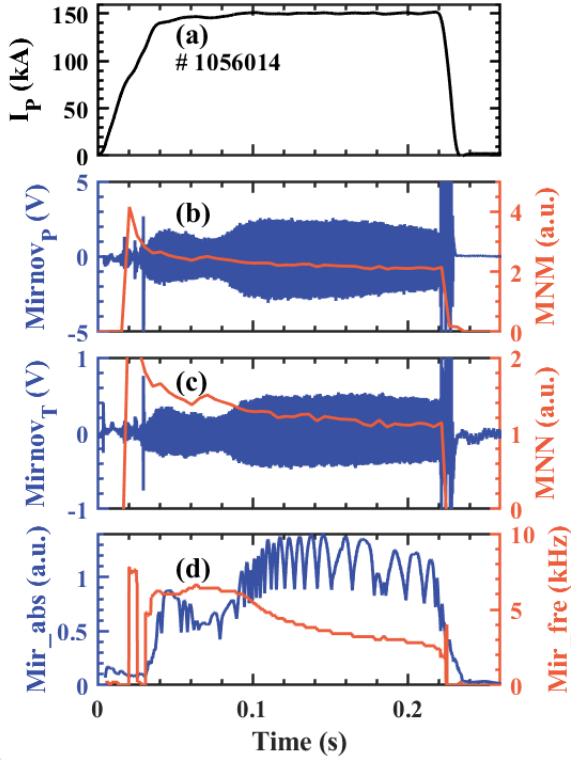


Figure 1 A typical disruptive discharge with tearing mode of J-TEXT. a) shows the plasma current of the discharge; b) and c) are the raw signal (left) and mode number (right) of the poloidal and toroidal Mirnov signals; d) shows *Mir_abs* (left) and *Mir_fre* (right) of one Mirnov signal (the raw signal in b)).

2.1.2 Radiation and density related features

Temperature hollowing and edge cooling are phenomena performance in profiles, which are 1D signals. In order to include the radial profiles of 1D signals in data-driven analyses, 0D peaking factor metrics have been synthesized on DIII-D¹⁹. Profile indicators³³ have also been applied on the transfer of adaptive predictors in JET and ASDEX Upgrade (AUG). Both the two methods are calculated the first order statistics, i.e. mean of the arrays. Deep learning models can extract 1D signals to features through convolution³⁰, which includes higher dimensional information. In our work, we calculated the higher-order statistics (HOS) of the 1D signals from the SXR, AXUV and FIR arrays for radiation and density related features.

Three HOSs have been selected to extract the 1D signals to 0D features: skewness (*skew*), and kurtosis (*kurt*). Variance (*var*) is a low-order statistic. As the variance (second) is higher-order than arithmetic mean (first), in this part the HOS is also included variance. Variance is a measure of dispersion, meaning it is a measure of how far a line of sight of the array is spread out from their average value. The plasma profiles are parabolic in distribution at the limiter configuration. The feature, *var* is defined by:

$$var = \frac{1}{n} \sum_{k=1}^n (x_k - \mu)^2 \quad (2-7)$$

where n is the number of lines in the array, x_k is the signal at the k^{th} line of sight in the array, μ is the mean of all signals in the array. Higher *var* represents the greater span of data in the profile. Therefore, higher *var* represents a more peaked profile, while lower *var* represents a more flat profile.

Skewness is a measure of the asymmetry of the distribution of the array signals about their mean. The feature, *skew* is defined by:

$$skew = \frac{\frac{1}{n} \sum_{k=1}^n (x_k - \mu)^3}{\left[\frac{1}{n} \sum_{k=1}^n (x_k - \mu)^2 \right]^{3/2}} \quad (2-8)$$

If *skew* > 0, the kind of skewness is called positive skew or right skewed state, which represents the mean > median > mode (statistics meanings) of the array signals. If *skew* < 0, then the opposite and if *skew* = 0, the three values above are the same. At the limiter configuration, The larger the *skew* the more the centre of gravity of the profile deviates from the centre of the plasma.

Kurtosis is a measure of the combined weight of a distribution's tails relative to the center of the distribution. The feature, *kurt* is defined by:

$$kurt = \frac{\frac{1}{n} \sum_{k=1}^n (x_k - \mu)^4}{\left[\frac{1}{n} \sum_{k=1}^n (x_k - \mu)^2 \right]^2} - 3 \quad (2-9)$$

"minus 3" is used to give a kurtosis of 0 to the normal distribution. This kind of kurtosis is also called excess kurtosis, which is simplified to kurtosis in this paper. Higher *kurt* indicates that there are fewer larger or smaller outliers and a more concentrated data distribution in the profile. Therefore, higher *kurt* represents a fatter profile, while lower *kurt* represents a thinner profile.

The HOS features in one discharge is shown in Figure 2. The blue line represents the 0D signal at the middle channel of each array, the green, yellow, and orange line represents *kurt*, *skew*, and *var*, respectively. In this discharge, the increase of plasma radiation lead to disruption. The increase on *var* of SXR array and AXUV array represents the radiation profile is gradually peaking. The slight reduction on *kurt* of FIR array indicates the gradient of density profile increased. The anomalous fluctuations in the *var*, *skew* and *kurt* before 0.15 ms are the result of the horizontal displacement of the plasma not yet fully stabilised.

Radiation related features also included the radiated power *P_rad* and 0D signals, which are impurities radiation *CIII* (carbon wall for J-TEXT) and soft x-ray radiation *SXR_core* at the middle channel. Density related features also included *sum_n_e* and 0D signal *n_e0*, line average density of the middle channel. The feature, *sum_n_e* is calculated by sum up all the

signals in FIR array to approximately express the electron density of the poloidal profile.

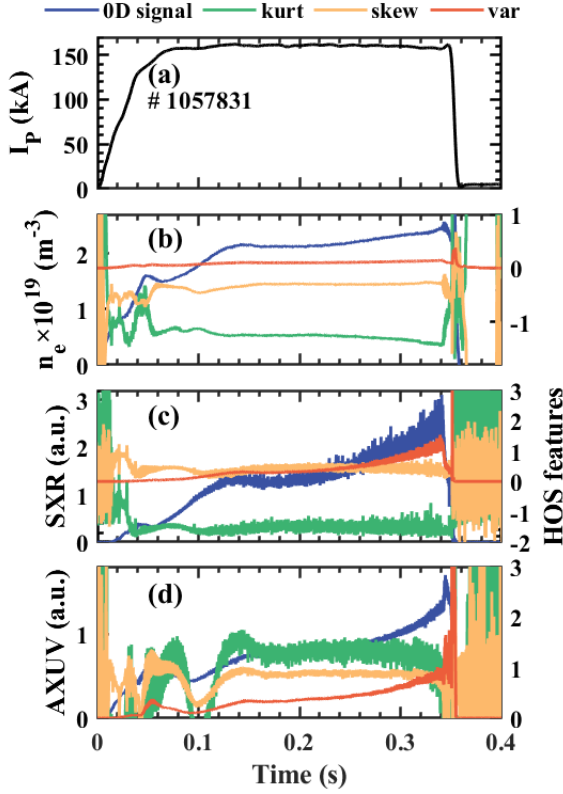


Figure 2 A disruptive discharge to show the HOS features in J-TEXT. The navy-blue line represents the OD signal at the middle channel of each array, the green, yellow, and orange line represents *kurt*, *skew*, and *var*, respectively. a) shows the plasma current of the discharge; b) shows the FIR array which provided density signals; c) shows the SXR array and d) shows the AXUV array which provided radiation signals.

2.2 Disruption classifier: Dropouts meet Multiple Additive Regression Trees (DART)

Tree-based models can be more accuracy than neural networks and linear models in many applications, such as tabular-style datasets, where features are individually meaningful⁴⁴. Features after PGFE are also individually meaningful for disruption prediction task. Gradient boosting decision tree (GBDT)⁴⁵ is a tree-based algorithm, which gives a prediction model in the form of an ensemble of weak prediction models, which are typically decision trees. Disruption prediction using LightGBM, which has been proposed based on GBDT has been introduced in our previous work^{27,28}. However, LightGBM and other GBDT based algorithm like Multiple Additive Regression Trees (MART) has the possibility of over-sensitive to the contributions of the few, initially added tress. This is not quite good enough in interpretability research, as it may lead to the model learning wrong knowledge. Dropouts meet Multiple Additive

Regression Trees (DART), which uses the trick of the dropout setting in deep neural networks⁴⁶ to randomly drop the existing decision trees and then iteratively optimise the boosted trees from the remaining set of decision trees could alleviate this problem. Therefore, DART, a tree-based model is selected as the disruption classifier of IDP-PGFE. There are two main differences between the DART algorithm and the GBDT based algorithm. First, when computing the gradient to be fitted to the nest tree, only a random subset of the existing set is selected with probability p_{drop} as the hyperparameter. Second, when DART adds a tree it needs to be normalised first. When adding the new tree without drop trees, the new tree should be scaled by a factor of $1/k$ to get the same order of magnitude as the dropped trees. Then the new tree and the dropped trees are scaled by a factor $k/(k+1)$ to ensure the effect before and after the new tree introduced remains the same. Where k is the number of trees dropped from the ensemble. If no tree is dropped, DART is in fact the traditional GBDT. If all trees are dropped, DART is equivalent to random forest (RF), because the regression tree has to be regenerated each time and there is no previous regression tree to base on.

2.3 Explainer: SHAP

SHAP is based on the game theoretically optimal Shapley values⁴⁷, which is a method from coalitional game theory to figure out how fairly distribute the "pay-out" (prediction) among the "players" (features). Shapley value is NOT the difference in prediction compared by removing feature(s) from the model. The Shapley value is the average contribution of a feature value to the prediction in different coalitions. SHAP is also an additive feature attribution method, which using a simpler explanation model as any interpretable approximation of the original model. Explanation models use simplified inputs x' that map to the original inputs through a mapping function $x = h_x(x')$. An explanation model g can be expressed as:

$$g(z') = \phi_0 + \sum_{j=1}^M \phi_j z'_j \quad (2-10)$$

Where $z' \in \{0,1\}^M$, $z'_j = 1$ means that the corresponding feature value is "present" and 0 that it is "absent". M is the number of simplified input features, and $\phi_j \in R$ is the feature attribution for a feature j , the Shapley values.

The Shapley values $\phi_j(f, x)$ is expressed as:

$$\phi_j(f, x) = \sum_{z' \subseteq x} \frac{|z'|!(M - |z'| - 1)!}{M!} [f_x(z') - f_x(z' \setminus j)] \quad (2-11)$$

where $|z'|$ is the number of non-zero entries in z' and $z' \setminus j$ denotes setting $z'_j = 0$. The Shapley values $\phi_j(f, x)$, explaining a prediction $f(x)$, are an allocation of credit among the features in x (the features extracted through PGFE) and are the only allocation satisfied three desirable properties. The first one is local accuracy, which ensure the explanation model g at least

match the predictor f . The second one is missigness to ensure features missing in the original input to have no impact, which means if $z' = 0$, the importance attributed is also 0. The third one is consistency (also called monotonicity in game theory researches), which states that if a feature is more important in one model than another, the importance attributed to that feature should also be higher.

SHAP is a unified approach to interpreting model predictions, which has the advantages of solid theoretical foundation in game theory, the only allocation of credit among the features and consistency of global and local interpretations. However, it is possible to create intentionally misleading interpretations with SHAP, which can hide biases⁴⁸, which need to be careful in explaining the predictor.

3. Dataset description

This section will describe the dataset selected to train, valid and test IDP-PGFE. The ECRH system was successfully commissioned at the beginning of 2019^{49,50}. The dataset of J-TEXT contains 1791 discharges out of 2017-2018 campaigns and 2021-2022 campaigns with the accessibility and consistency of the diagnostics channels, including discharges applied ECRH and RMPs. All types of disruptions were included except intentional ones triggered by MGI or SPI and engineering tests. 212 disruptive and 1199 non-disruptive discharges are selected as the training set. 80 disruptive and 80 non-disruptive discharges are selected as the validation set. 110 disruptive and 110 non-disruptive discharges are selected as the test set. Both training and validation set are selected randomly from 2017-2018 campaigns. The test set is selected randomly from 2017-2018 and 2021-2022 campaigns to simulating real operating scenarios. The locked mode detectors in 2017-2018 campaigns are ex-vessel saddle loops, while in 2021-2022 campaigns are B_r HFS Mirnov probes⁴³. The Mirnov probes in poloidal array in 2017-2018 campaigns are belong to poloidal probe array 1, while in 2021-2022 campaigns are belong to poloidal probe array 2. Split of datasets are shown in table 2. All discharges are split into slices from the platform of plasma current to CQ time per 0.1 ms, the same of the sampling rate of plasma current in J-TEXT. A time threshold equaled to 25 ms before CQ time indicates the unstable phase of each disruptive discharge. The time threshold is determined by finding the best performance of our model through scanning the time threshold from 5 ms to 50 ms. The "unstable" slices in disruptive charges are labelled as "disruptive", and all the slices in non-disruptive discharges are labelled as "non-disruptive". The disruptive slices are totally from part from the disruptive discharges, and the non-disruptive slices are from all the non-disruptive discharges, which lead to the great imbalance of the dataset. Therefore, we increased the weights of disruptive slices and dropped a portion of non-disruptive slices randomly to make a balance between the two kinds of slices.

Table 2 Split of datasets of the predictor

	Non-disruptive	Disruptive
No. training shots	1199	212
No. validation shots	80	80
No. test shots	110	110

4. Predictive performances of IDP-PGFE

This section shows the high performance and low data required abilities of IDP-PGFE based on PGFE. Disruption prediction is a binary classification task, of which confusion matrix is often used to evaluate the performance. In disruption prediction, True positive (TP) refers to a successfully predicted disruptive discharge. False positive (FP) refers to non-disruptive discharge predicted as disrupted, which is also called false alarm. True negative (TN) refers to a non-disruptive discharge predicted as non-disruptive too. False negative (FN) refers to a disruptive discharge not predicted as disruptive, which contains miss alarm and tardy alarm. Short warning time should be reckoned as tardy alarm, due to the requirement of disruption mitigation system. In IDP-PGFE, any predicted disruption with a warning time less than 10 ms is reckoned as FN. The evaluation indicators of a disruption predictor are receiver operating characteristic curve (ROC), which included true positive rate (TPR), false positive rate (FPR) and area under ROC curve (AUC). TPR, FPR and F -score are calculated as follows:

$$TPR = \frac{TP}{TP + FN} \quad (4-1)$$

$$FPR = \frac{FP}{FP + TN} \quad (4-2)$$

The DART will give a result between "0" ("non-disruptive") and "1" ("disruptive"), which can be binarily classified by manually setting a model threshold. Each model threshold corresponds to a set of TPR and FPR. The ROC curve is created by plotting TPR against FPR at various threshold settings.

Disruption predictors are often disturbed by anomalous features and lead to false alarms or lucky guess, which means the warning time may just the non-physics perturbations on the features. To reduce or avoid this, an alarm threshold strategy is adopted on IDP-PGFE. The actual warning time is determined by the binarily classified predicted result and an alarmed time threshold. The during time of predicted result as "disruptive" consecutively should larger than alarmed time threshold, then the warning time is the latest time of the consecutively alarm time. For example, if alarmed time threshold is set to 5ms, the predicted result needs to be "disruptive" for 5ms consecutively to be defined as a prediction of "disruptive". A larger alarmed time threshold will give higher stability to the predictor, but will also result in shorter alarm times for the prediction. Therefore, different

alarmed time threshold strategies need to be set to meet the different demands of the disruption predictor.

In this section, the performances of IDP-PGFE are reported in detail for J-TEXT. In section 4.1, the results of the full data under different alarmed time threshold strategies are described. As described in introduction, PGFE has the ability on few shots learning. The cases of few shots learning via IDP-PGFE with less data are addressed in section 4.2.

4.1 IDP-PGFE performances on J-TEXT

In this part, IDP-PGFE was trained with full data. The performances of IDP-PGFE for three alarmed time threshold strategies and a benchmark disruption predictor using raw signals (DPRS) are shown in figure 3. The navy-blue line represents the ROC curve of predictor using raw signals. The others represent the ROC curves of IDP-PGFE under different alarmed time threshold strategies. The hyperparameters of each best performance model are determined by the hyperparameter search. Although, the AUC value of DPRS is 0.935, the performances of IDP-PGFE under all alarmed time threshold strategies are much better than it. Because DPRS actually does not include a feature extractor, while PGFE plays the role of feature extractor in IDP-PGFE. This leads to the conclusion that the PGFE-based IDP-PGFE is superior in predictive performance to a disruption predictor using the raw signals.

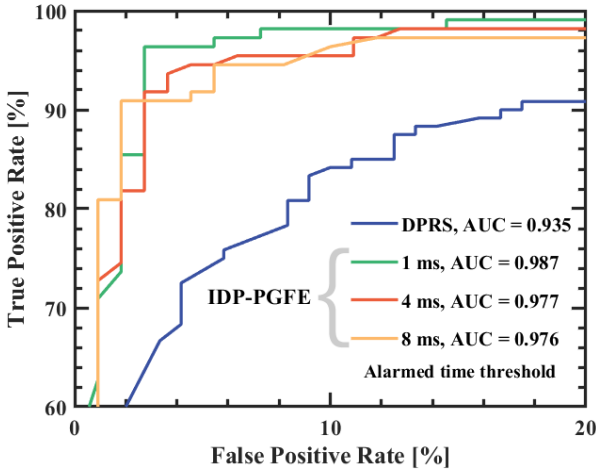


Figure 3 The ROC curves of IDP-PGFE under different alarmed time threshold strategies and DPRS. The FPR axis is from 0% to 20%, the TPR axis is from 60% to 100%. The navy-blue line represents the ROC curves of predictor using raw signals. The others represent the ROC curves of IDP-PGFE under different alarmed time threshold strategies (alarmed time threshold = 1ms – green, alarmed time threshold = 4ms – orange, alarmed time threshold = 8ms – yellow). The performances of IDP-PGFE under all alarmed time threshold strategies are better than DPRS.

The alarmed time threshold strategies does not have a significant effect on the overall performance of the model, with a slight decrease in AUC values as alarmed time threshold increases. This phenomenon means that the predictive performance of IDP-PGFE is very stable and less susceptible to false alarms caused by feature perturbations.

When the model threshold is fixed, alarmed time threshold strategies will also affect the accumulated percentage of disruption predicted versus warning time. Figure 4 shows the accumulated percentage of disruption predicted versus warning time with the fixed model threshold = 0.5. Four coloured solid lines represent three alarmed time threshold strategies, respectively. There is an overall advance in warning time as alarmed time threshold increases. Due to J-TEXT is a small-sized tokamak with a relatively smaller time scale for disruption to take place, the warning time of J-TEXT is shorter than that for JET, EAST, DIII-D or other large and medium sized tokamaks. The setting of model threshold and alarmed time threshold depends on the distribution of warning time. On one hand, if the warning time larger than 300ms in J-TEXT, the successfully prediction should be regarded as lucky guess. Although, lucky guess is an acceptable prediction for disruption prediction, it is not an economical prediction for future reactors. On the other hand, only electromagnetic particle injector (EPI) could react by the trigger advanced 10ms. Therefore, the warning time of 30ms should also make sure a considerable accumulated percentage of disruption predicted for other disruption mitigation methods to react. The final performance of IDP-PGFE is TPR = 97.27%, FPR = 5.45% with a tolerance of 10ms under the model threshold = 0.5, alarmed time threshold = 1ms, considering the reduction in lucky guess and the guaranteed warning time. The TPR could reach 94.55% with a tolerance of 20ms, and 90% with a tolerance of 30ms.

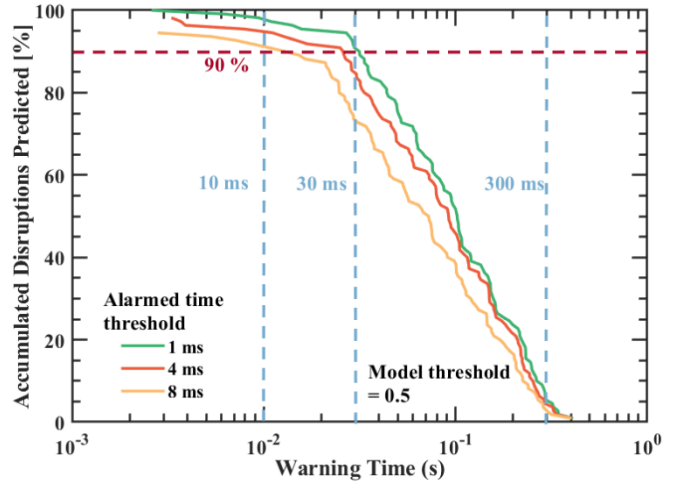


Figure 4 The accumulated percentage of disruption predicted versus warning time. The model threshold is fixed as 0.5, three alarmed time threshold strategies are the same as figure 3 described above. Four coloured solid lines represent three

alarmed time threshold strategies, respectively (alarmed time threshold = 1ms – green, alarmed time threshold = 4ms – orange, alarmed time threshold = 8ms – yellow). The red dashed line represents the accumulated percentage of disruption predicted equals to 90%. The light blue dashed lines represent the warning time of 10ms, 30ms and 300ms.

4.2 Low data required learning via IDP-PGFE

In this part, IDP-PGFE was trained with less data, which are 80%, 60%, 40%, 20%, 10%, 5%. The model threshold = 0.5 and alarmed time threshold = 1ms. The hyperparameters of each best performance model are determined by the hyperparameter search. The ROC curves of IDP-PGFE trained by 100% (full), 60%, 40%, 10%, 5% data sizes and DPRS are shown in figure 5. The navy-blue line represents the ROC curve of predictor using raw signals, the deep-red line represents the ROC curve of IDP-PGFE with full data. As the training data size decreases, the performance of IDP-PGFE degrades. The performance of IDP-PGFE with 10% data size reaches that of DPRS. However, the performance of IDP-PGFE with 5% data size degrades significantly. IDP-PGFE with 10% data size is still acceptable as a disruption predictor (AUC = 0.939, the best TPR = 89.09%, FPR = 10%), whereas with 5% data size is not (AUC = 0.845, the best TPR = 75.45%, FPR = 15.45%).

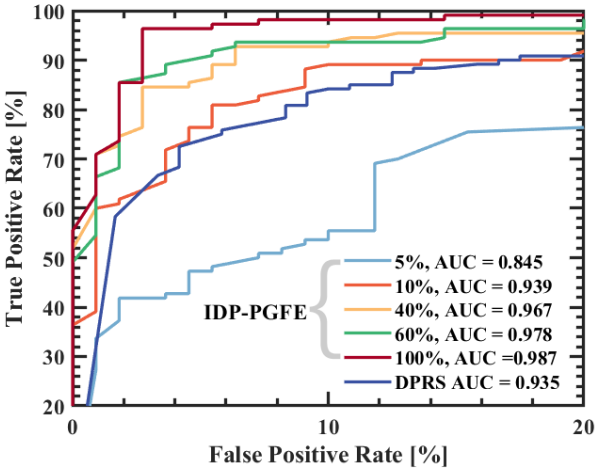


Figure 5 The ROC curves of IDP-PGFE trained by different data sizes and DPRS. The FPR axis is from 0% to 20%, the TPR axis is from 20% to 100%. The navy-blue line represents the ROC curve of predictor using raw signals. Five coloured lines represent five kinds of data size, respectively (100% – deep-red, 60% – green, 40% – yellow, 10% – orange, 5% – light-blue). The AUC value of IDP-PGFE with 10% data size is similar to the AUC value of DPRS. The AUC value of IDP-PGFE with 5% data size is the smallest.

The few shots learning ability is not benefit from the disruption classifier DART, but from the feature extractor

PGFE. DPRS was also trained with less data as a benchmark. The evolution of the AUC values with the training data size is shown in figure 6. The orange line represents IDP-PGFE, the navy-blue line represents DPRS. As the training data size decreases, the performance of DPRS degrades faster than that of IDP-PGFE. The performance of IDP-PGFE and DPRS has significant reduction at 10% data size and 20% data size, respectively. It is worth noticing that the 10% data size including about 20 disruptive discharges and 120 non-disruptive discharges, which are quite a small data requirement for disruption prediction task. PGFE as a feature extractor could obviously reduce the data requirement of the disruption predictor by the feature extraction specific to tokamak disruption.

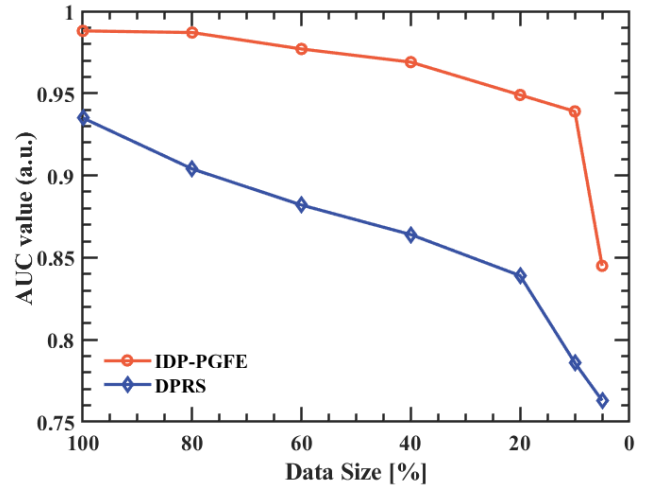


Figure 6 The AUC value versus data size of the training set for two kinds of models. The navy-blue line represents DPRS. The orange line represents IDP-PGFE. The x-axis decreases from 100% to 5%. The AUC value of DPRS decreases faster than that of IDP-PGFE as the data size decreases. The AUC value of IDP-PGFE ramps down from 0.939 to 0.845 with the data size from 10% to 5%, while the AUC value of DPRS ramps down from 0.839 to 0.763 with the data size from 20% to 5%.

5. Interpretability study and the application on J-TEXT experiments

This section will describe the interpretability study by IDP-PGFE and the application on J-TEXT disruption experiments. The interpretability application is not setting real-time disruption prediction, but analysing and providing new understanding of the exist experiment phenomena. The interpretability study of IDP-PGFE could also help physicist find directions for further analysis of the experiment. Section 5.1 and 5.2 will describe the applications on ECRH and RMP experiment, respectively.

The outstanding performance of IDP-PGFE can somewhat reflect the fact that IDP-PGFE has learned enough correct knowledge related to J-TEXT disruption, otherwise it would

not be possible to have such a high accuracy. Moreover, by checking the model interpretation results with widely accepted disruption precursors can also act as a test to verify the model has learned physically meaningful pattern instead of some leaked information in the data. Nevertheless, understanding how IDP-PGFE recognize "disruptive" and "non-disruptive" is more important, which may even provide us new understanding of disruption. A new connection between the algebraic and geometric structure of knots has been discovered by using attribution techniques²². Attribution techniques help people understand the relations between mathematical objects by providing the contributions of the mathematical objects. SHAP is also an attribution technique could not only provide the contributions of features but also provide how feature value impact on model output. Figure 7 shows the SHAP value of different features and their relations with feature value. We will study the interpretability of IDP-PGFE still from the four categories of the PGFE, MHD instabilities, radiation, density related features and basic PCS signals.

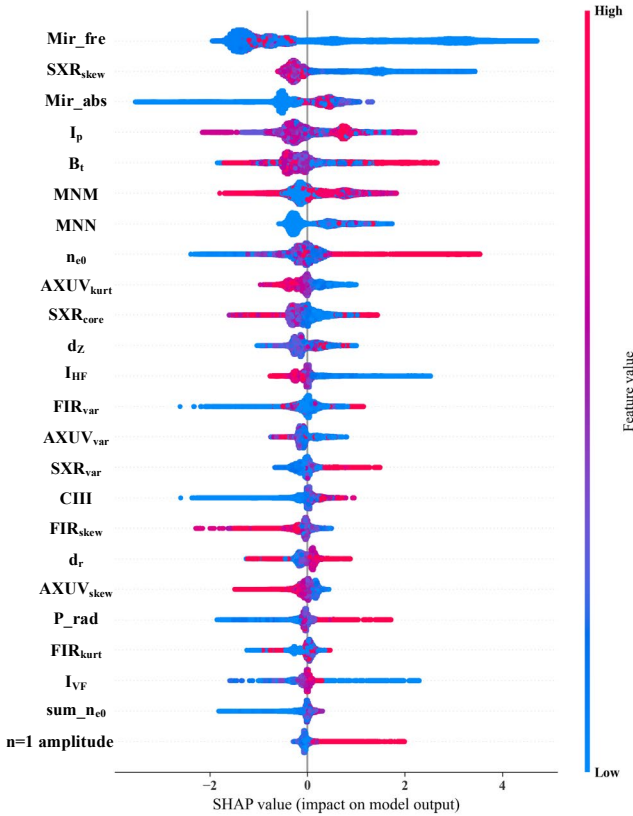


Figure 7 The SHAP value of different features and their relations with feature value. The order of the features represents the contributions of features. The colormap represents the feature value of each feature, red means high and blue means low. Positive SHAP value represents "disruptive" impact on model, while negative SHAP value represents "non-disruptive" impact on model.

MHD instabilities related features: The frequency of Mirnov probe Mir_fre reflected the frequency of MHD instabilities is the most contributed feature. Lower value of Mir_fre may both contribute to "disruptive" and "non-disruptive". If the frequency of the Mirnov probe slowdown, the contribution is to "disruptive", which reflects the locked mode process. Otherwise, if the frequency of the Mirnov probe is always about to 0, the contribution is to "non-disruptive", which reflects there is no MHD instabilities. Higher value of Mir_fre contributes more to "non-disruptive", which means the high-speed rotating mode is not the direct reason to disruption. The two cases can be distinguished by the 3rd ranked contribution feature, the intensity of Mirnov probe Mir_abs . Lower value of Mir_abs contribute more to "non-disruptive", which represent the no MHD instabilities case. J-TEXT is a small-sized tokamak with a relatively smaller time scale not only for disruption but also for LM to take place. Therefore, $n = 1$ amplitude is not an effective time-sensitive disruption precursor, as the typical discharge shown in section 2.1.1. The $n = 1$ amplitude is the 24th ranked contribution feature and higher value contributes more "disruptive". MNM is 6th ranked contribution feature and higher value of MNM ($m > 2$) both contribute more to "disruptive" and "non-disruptive". The case that contributes more to "disruptive" may relate to multi-magnetic island overlaps, while the other case may relate to edge magnetic island which even could improve the plasma confinement [island divertor]. MNN is 7th ranked contribution feature and higher values of MNN mixed in lower value contributes more to "disruptive" may also relate to multi-magnetic island overlaps such as 2/1 and 3/2 coupling caused disruption in J-TEXT⁵¹.

Radiation related features: The 2nd ranked contribution feature is SXR_skew and lower value of SXR_skew contributes more to "disruptive". lower value of SXR_skew does not mean that the soft x-ray radiation is high. Figure 8 shows the SHAP value of SXR_skew with respect to the value of SXR_skew and SXR_core . This figure shows that only with lower SXR_core and lower SXR_skew together is more contributed to "disruptive", which reflects the general decrease of soft x-ray radiation. The 15th ranked contribution feature is SXR_var and higher value of SXR_var represents more peaked profile, which contributes more to "disruptive". This is usually a precursor to the density limit disruption. The 9th ranked contribution feature is $AXUV_kurt$ and lower value of $AXUV_kurt$ represents more thinner profile, which contributes more to "disruptive". The thinner profile usually represents larger gradients of the profile. The 20th ranked contribution feature is P_rad and higher value of P_rad represents more losses of plasma radiation energy, which contributes more to "disruptive". The other radiation related features do not contribute significantly and their values also do not discriminate significantly will not describe in detail here.

Density related features: The density related features are intuitive to understand. The most contribution feature among the density related features is n_{e0} , which is the 8th ranked contribution feature. Higher value of n_{e0} represents the density limit disruption. No matter how FIR_{var} , FIR_{skew} and FIR_{kurt} contribute, J-TEXT cannot escape the density limit disruption after all. The higher value of FIR_{var} and lower value of FIR_{skew} contribute more to "disruptive" could provide more detailed information of the density limit disruption, which are more peaked density profile and more general increase of plasma density, respectively.

Basic PCS signals: It is very interesting to note that I_p and B_t get the 4th and 5th ranked contribution feature, respectively. Even if I_p and B_t do not changes a lot in one discharge, their contribution is still large because they are basic parameters of plasma. The value of I_p and B_t along has no impact on "disruptive" or "non-disruptive". Both d_z and I_{HF} could reflect the vertical displacement, lower value of I_{HF} represent the out of control of vertical displacement, which contributes more to "disruptive". Both d_r and I_{VF} could reflect the horizontal displacement, higher value of d_r both contribute more to "disruptive" and "non-disruptive" may represent that in J-TEXT the horizontal displacement to LFS limiter is salvageable.

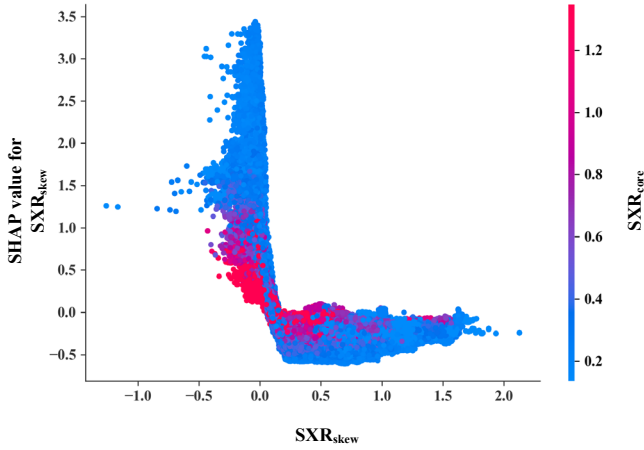


Figure 8 The SHAP value of SXR_{skew} with respect to the value of SXR_{skew} and SXR_{core} . The x-axis represents the value of SXR_{skew} ; the colormap represents the value of SXR_{core} ; the y-axis represents the SHAP value of SXR_{skew} .

The analysis above is only the preliminary study on the interpretability of IDP-PGFE, much of the analysis is speculative and not conclusive. Even the study is preliminary, it still brings new understanding to the J-TEXT experiments. The next two parts will introduce the interpretability applications on J-TEXT experiments based on the preliminary study.

5.1 Interpretability application on ECRH experiment

The experiments that investigating the influence of ECRH on disruption due to continuously increasing density towards density limit in J-TEXT has been carried out in 2021 spring. In the ECRH experiments ($I_p = 120$ kA, $B_t = 1.7$ T, $P_{ECRH} = 100$ -300 kW, $r_{ECRH} = 10.2$ cm) it is found that the application of ECRH lower the density limit at disruption with two different reproducible experimental phenomena. Three typical discharges in this experiment have been selected in the text set and their overviews of the experiment are shown in figure 9. The discharge without the application of ECRH reached the highest density limit about $0.79n_G$. The discharges with the application of 300 kW ECRH only reached the density limit about $0.69n_G$ and $0.56n_G$. In #1074395 discharge, after the application of ECRH, disruption occurred soon when density reached $0.69n_G$. In #1074399 discharge, MHD instabilities appeared after the application of ECRH. As soon as ECRH cut off, disruption occurred when density reached about $0.56n_G$. It is difficult to conclude from the available experimental phenomena whether ECRH has actually lowered the density limit or whether the disruption was caused by other reasons before the density limit was reached.

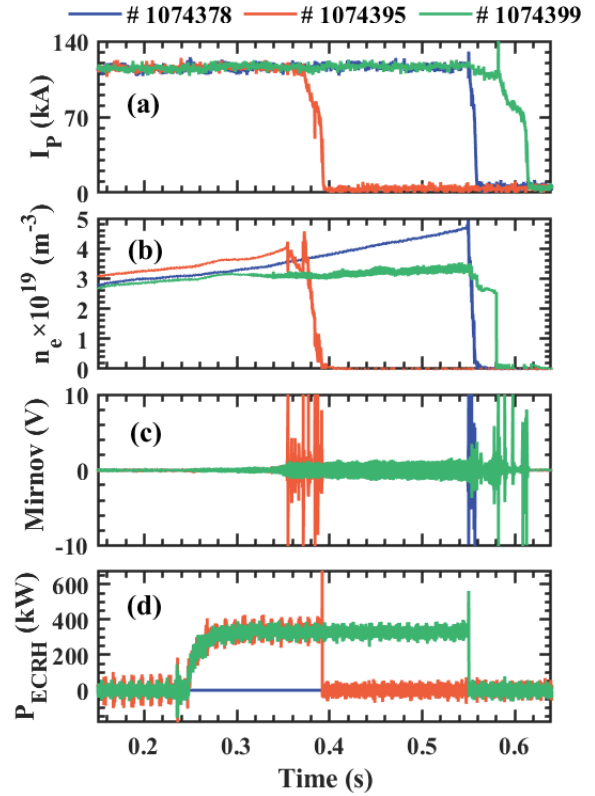


Figure 9 The overview of the three typical discharges in J-TEXT disruption experiment under ECRH. The blue line represents the discharge without the application of ECRH with the density limit about $0.79n_G$. The orange line and green line represent the discharge with the application of 300 kW ECRH with the density limit about $0.69n_G$ and $0.56n_G$, respectively. a) shows the plasma current of three discharges; b) shows the line average density of middle channel; c) shows the Mirnov signal; d) shows the ECRH power.

d) shows the ECRH power. It needs to notice that in # 1074395 discharge, the ECRH cut off due to the disruption, while in # 1074399 discharge, disruption occurred after the ECRH cut off.

Figure 10, figure 11 and figure 12 show the predicted result, SHAP value and four typical features in #1074378, #1074395 and #1074399 discharges, respectively. The #1074378 discharge is a typical density limit disruption discharge, the predicted result increased because of the increase of SHAP value of n_{e0} . The SHAP value of MNM increased close to disruption which coincides with the rapid onset of MHD instabilities prior to density limit disruption.

In #1074395 discharge, the SHAP value of P_{rad} increases after the application of ECRH, however, this only contributes little to the predicted result. At about 0.33s, onset of MHD instabilities (possibly $m = 3$ and $m = 2$ mode coupling) appeared⁵¹, which contributed to the predicted result a little. The significant contribution is Mir_{abs} which raised the predicted result larger than 0.5. Therefore, this discharge is not a density limit disruption and the application of ECRH do not lower the density limit in this case.

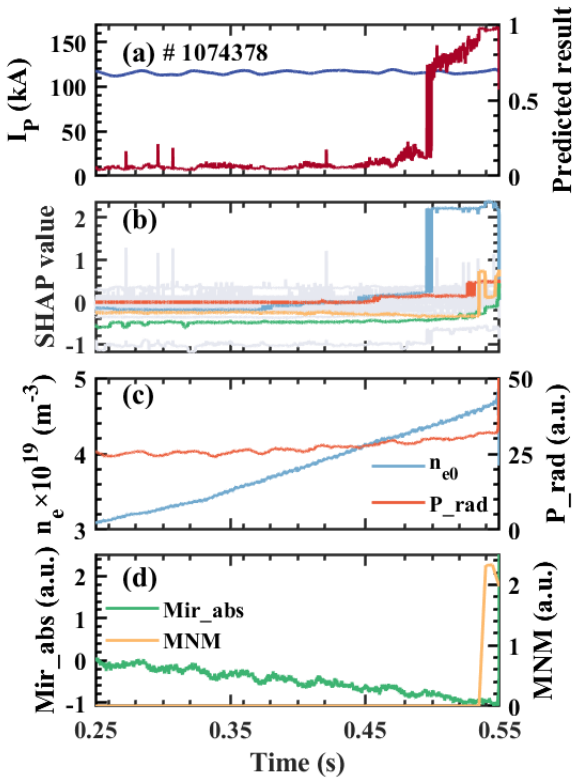


Figure 10 The predicted result, SHAP value and four typical features in # 1074378 discharge without the application of ECRH. a) shows the plasma current and predicted result; b) shows the SHAP value of all the features, the coloured lines represent the four typical features; c) shows two typical features, line average density of the middle channel n_{e0} (light blue) and the radiated power P_{rad} (orange); d) shows two

typical features, the intensity of Mirnov probe Mir_{abs} (green) and the poloidal mode number MNM (yellow).

In #1074399 discharge, the SHAP value of P_{rad} also increases after the application of ECRH like the case before. At about 0.32s, onset of MHD instabilities (still possibly $m = 3$ and $m = 2$ mode coupling) also appeared, which contributed to the predicted result a lot through the feature Mir_{fre} and caused an early alarm. However, in this case disruption did not occur at once, but occurred after the ECRH cut off. The SHAP value of Mir_{abs} were the mainly contribution to predicted result after the early alarm, which caused alarming continuously in this discharge. Obviously, this discharge is still not a density limit disruption and the application of ECRH do not lower the density limit.

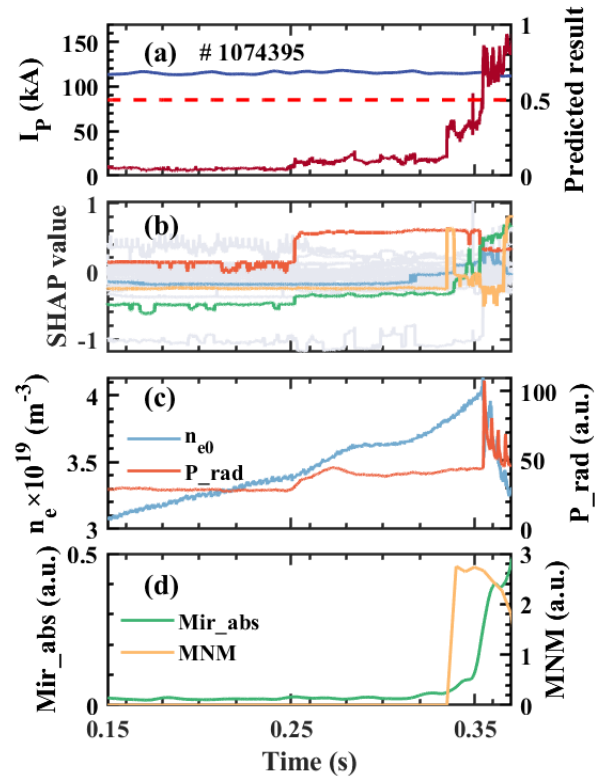


Figure 11 The predicted result, SHAP value and four typical features in # 1074395 discharge with the application of ECRH at 0.25 s. a), b), c) and d) show the same as figure 10.

Through the interpretability study of these three typical discharges, it can conclude that the application of ECRH do not lower the density limit but causes other types of disruption. Two directions for further analysis of the experiment can also be found by the understanding above. First, the relationship between radiated power and MHD instabilities requires an in-depth study, which may be similar to the density limit disruption in physical mechanisms. Second, in # 1074399 discharge the appearing of the MHD instabilities caused an early alarm and the application of ECRH delay the disruption

caused by the MHD instabilities. The difference of the MHD instabilities between these two cases is worth investigating.

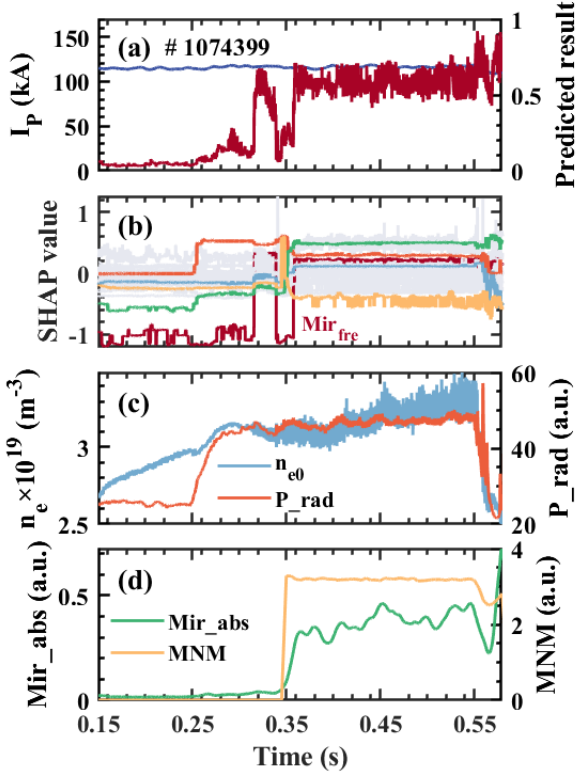


Figure 12 The predicted result, SHAP value and four typical features in # 1074399 discharge with the application of ECRH at 0.25 s. a), b), c) and d) show the same as figure 10.

5.2 Interpretability application on RMP experiment

The experiments that investigating the influence of RMPs on disruption due to continuously increasing density towards density limit in J-TEXT has been carried out in 2022 spring. In the RMP experiments ($I_p = 120$ kA, $B_t = 2.1$ T, $I_c = 0-4$ kA) it is found that the application of RMPs raised the density limit at disruption. Two typical discharges in this experiment have been selected in the text set and their overviews of the experiment are shown in figure 13. The discharge without the application of RMP also reached the density limit about $0.79n_G$. In the RMP experiment, the discharges with the application of 2 kA RMPs reached the highest density limit about $0.91n_G$, which is a really high density limit in J-TEXT. The #1080564 discharge is a typical high q_a density limit disruption discharge, multifaceted asymmetric radiation from the edge (MARFE) and detached plasma reflected in the ratio evolution of the line integral density at HFS to that at LFS^{52,53}. As the density continuing to rise, the ratio began to increase along with the onset of MARFE then decreased when detached plasma happened. The application of RMPs delay the decrease of the ratio, as a result in raising the density limit and delay the disruption in #1080550 discharge. The

interpretability study of IDP-PGFE could help physicist to confirm if the application of RMP really raised the density limit and find out the possible reason.

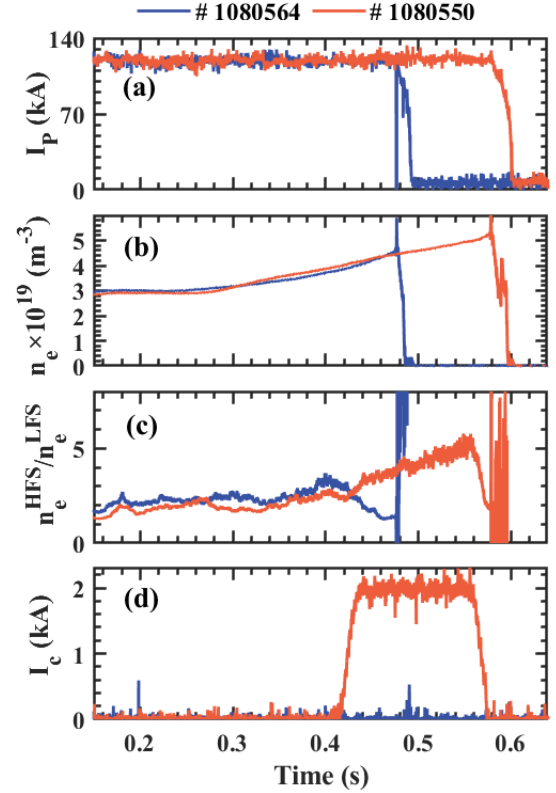


Figure 13 The overview of the two typical discharges in J-TEXT disruption experiment under RMPs. The blue line represents the discharge without the application of RMPs with the density limit about $0.79n_G$. The orange line represents the discharge with the application of 2 kA RMPs with the density limit about $0.91n_G$. a) shows the plasma current of three discharges; b) shows the line average density of middle channel; c) shows the ratio of the line integral density at HFS to that at LFS; d) shows the RMPs current. Disruption occurred after the RMPs cut off.

Figure 14 and figure 15 show the predicted result, SHAP value and four typical features in #1080564 and #1080550 discharges, respectively. The #1080564 discharge is a high q_a density limit disruption discharge different from #1074378, the predicted result increased because of the increase of SHAP value of $CIII$, $AXUV_{kurt}$ and MNM . The SHAP value of n_{e0} increased only close to disruption. The SHAP value of $CIII$ increased at about 0.39s (during MARFE) contributed the predicted result to about 0.4. At about 0.42s detached plasma happened, the SHAP value of $AXUV_{kurt}$ increased with the value of $AXUV_{kurt}$ decreased, which represents a thinner profile. This contributed to the predicted result a lot. At about 0.44s, the SHAP value of MNM increased and contributed the predicted result larger than 0.5. The interpretability study in the high q_a density limit disruption discharge shows that

before the density limit disruption, detached plasma and MHD instabilities could be the reason of density limit disruption⁵².

In #1080550 discharge, The SHAP value of $CIII$ still increased at about 0.39s (during MARFE). However, because of the application RMPs, detached plasma did not happen. Therefore, the value of $AXUV_{kurt}$ did not decrease so that the SHAP value of $AXUV_{kurt}$ did not increased. The most significant contribution to predicted result is n_{e0} because in the view of IDP-PGFE, this discharge reached the density limit. After RMPs cut off, at about 0.56s the value of $AXUV_{kurt}$ decreased and MNM increased, which means the detached plasma and MHD instabilities appeared again and caused the disruption.

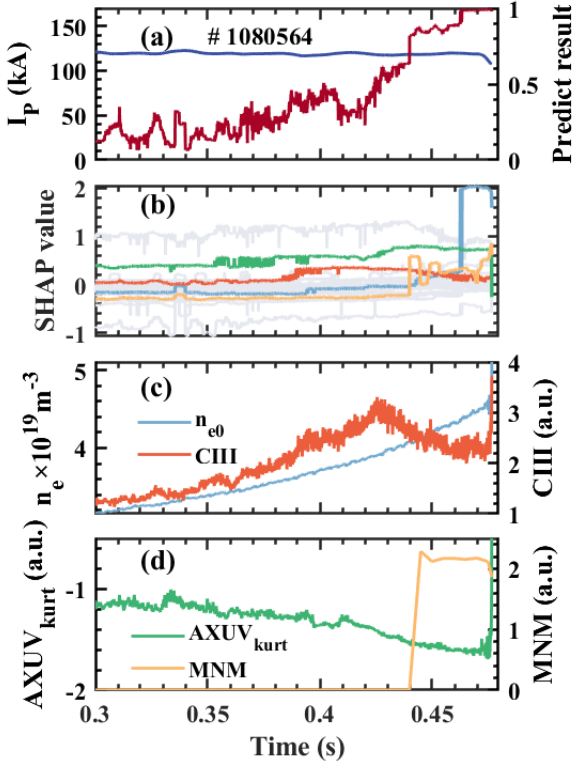


Figure 14 The predicted result, SHAP value and four typical features in # 1080564 discharge without the application of RMPs. a) shows the plasma current and predicted result; b) shows the SHAP value of all the features, the colored lines represent the four typical features; c) shows two typical features, line average density of the middle channel n_{e0} (light blue) and the impurities radiation $CIII$ (orange); d) shows two typical features, the kurtosis of AXUV array $AXUV_{kurt}$ (green) and the poloidal mode number MNM (yellow).

Therefore, the application of RMPs really raise the density limit by delaying detached plasma and MHD instabilities before the density limit disruption. It is found that the application of RMPs not only has the impact on MHD instabilities as investigated before⁵⁴, but also has the impact

on radiation profile ($AXUV_{kurt}$). The contribution of $AXUV_{kurt}$ and MNM is more significant than the contribution of n_{e0} . This is a new understanding of the RMP experiment on the density limit disruption, which could guide physicist figure out the physical mechanisms of the density limit disruption.

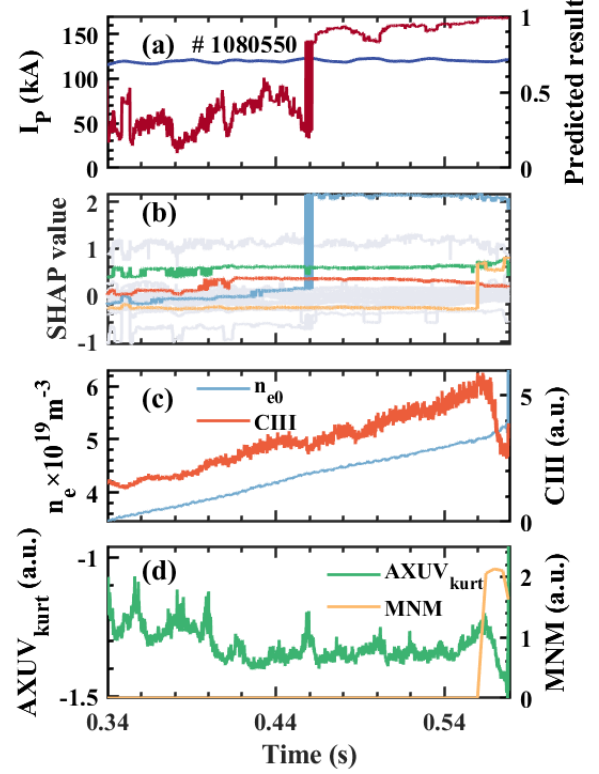


Figure 15 The predicted result, SHAP value and four typical features in # 1080550 discharge with the application of RMPs. a), b), c) and d) show the same as figure 14.

6. Discussion

This section will discuss the potentials and limitations of IDP-PGFE. We will discuss in three topics: interpretability, transferability and feasibility of real-time.

Interpretability

A new connection between the algebraic and geometric structure of knots has been discovered by a process proposed by DeepMind²². The process has three steps, first using machine learning to discover potential patterns and relations between mathematical objects; second, understanding them with attribution techniques; third, using these observations to guide intuition and propose conjectures. In IDP-PGFE, PGFE as a feature extractor extracts the disruptive-related features (mathematical objects), DART as a disruption classifier is the machine learning tool to discover potential patterns and relations between features, SHAP is the attribution techniques as an explainer to understand the potential patterns and relations between features, has finished the first and second steps. It means that IDP-PGFE has the potential for propose

new conjectures of disruption. We guided intuition on density limit disruption and propose the new conjecture that the application of RMPs can raise the density limit, while the application of ECRH cannot in J-TEXT. More new conjectures and physical mechanisms of disruption requires in-depth collaboration with physicists in the future.

However, the limitation is based on the dataset and PGFE. The dataset is only the J-TEXT dataset, therefore, IDP-PGFE could only learn the disruption existing on J-TEXT. Larger dataset with various disruption types and plasma configurations is more helpful in interpretability of disruption prediction. The feature extraction techniques of PGFE are not ultimate. Inverted plasma profiles, more physics features and other inductive bias of disruption could make PGFE more powerful.

Transferability

IDP-PGFE has an advantage on the low data requirement, therefore, IDP-PGFE could directly train on the target dataset. However, the even if the training set only required 10%, it still included about 20 disruptive discharges and 120 non-disruptive discharges. The transferability of IDP-PGFE need to use domain adaption technique, which is also our future plan.

Feasibility of real-time

IDP-PGFE is based on tree models, which is an advantage in real-time disruption prediction. Meanwhile, PGFE make the diagnostic signals into diagnostic-independent features, which means the lack of diagnostic signals is not so serious to IDP-PGFE. IDP-PGFE also has the potential for disruption avoidance and prevention via real-time SHAP value.

7. Summary

This paper introduced an interpretable disruption predictor based on physics-guided feature extraction (PGFE) called IDP-PGFE. IDP-PGFE is made up of a feature extractor, a disruption classifier and an explainer, which are based on PGFE, DART and SHAP, respectively. PGFE extracts features with the inductive bias that related to MHD instabilities, radiation and density caused disruptions based on the comprehension of phenomena. DART is a tree-based model using the trick of the dropout, which can reduce the overfitting. SHAP is an attribution technique, which using a simpler explanation model as any interpretable approximation of the original model. IDP-PGFE reaches the best performance in J-TEXT disruption prediction task benefit from PGFE. The performance of IDP-PGFE is TPR = 97.27%, FPR = 5.45% with a tolerance of 10ms. The TPR could reach 94.55% with a tolerance of 20ms, and 90% with a tolerance of 30ms. PGFE could also reduce the data requirement of IDP-PGFE. The performance of IDP-PGFE using PGFE with only 10% data size of the training dataset is similar to the performance of disruption predictor using raw signals with full training dataset.

The analysis on the contribution of features given by SHAP not only generally consistent with existing comprehension, but also helped understanding some of the J-TEXT disruption process. The interpretability application provides the analysis and new understanding of the exist experiment phenomena. It helps physicists to confirm that the application of ECRH did not lower the density limit, while the application of RMPs did raise the density limit of J-TEXT density limit disruption. The interpretability study of IDP-PGFE could also guide intuition on the physical mechanisms of density limit disruption that RMPs not only effect the MHD instabilities but also the radiation profile, which delay the density limit disruption. Last but not least, we give a brief discussion in three topics, interpretability, transferability and feasibility of real-time to discussion the potentials and limitations of IDP-PGFE. IDP-PGFE has the potentials for propose new conjectures of disruption, transfer to other tokamaks via domain adaption technique and disruption avoidance and prevention.

Acknowledgement

This work was supported by National Key R&D Program of China under Grant (No. 2022YFE03040004, No. 2018YFE0310300 and No. 2019YFE03010004) and by National Natural Science Foundation of China (NSFC) under Project Numbers Grant (No. 12075096 and No. 51821005).

References

1. Hender, T. C. *et al.* Chapter 3: MHD stability, operational limits and disruptions. *Nucl. Fusion* **47**, S128–S202 (2007).
2. Boozer, A. H. Theory of tokamak disruptions. *Physics of Plasmas* **19**, 058101 (2012).
3. Sugihara, M. *et al.* Disruption scenarios, their mitigation and operation window in ITER. *Nucl. Fusion* **47**, 337–352 (2007).
4. de Vries, P. C. *et al.* Requirements for Triggering the ITER Disruption Mitigation System. *Fusion Science and Technology* **69**, 471–484 (2016).
5. de Vries, P. C. *et al.* Survey of disruption causes at JET. *Nucl. Fusion* **51**, 053018 (2011).
6. Berkery, J. W., Sabbagh, S. A., Riquezes, J. D., Gerhardt, S. P. & Myers, C. E. Characterization and forecasting of global and tearing mode stability for tokamak disruption avoidance. 4.
7. Berkery, J. W., Sabbagh, S. A., Bell, R. E., Gerhardt, S. P. & LeBlanc, B. P. A reduced resistive wall mode kinetic stability model for disruption forecasting. *Physics of Plasmas* **24**, 056103 (2017).
8. Sabbagh S.A. *et al.* 2018 Disruption event characterization and forecasting in tokamaks

- Preprint: 2018 IAEA Fusion Energy Conf. (Gandhinagar, India, 22–27 October 2018) [EX/P6-26] (<https://conferences.iaea.org/event/151/contributions/5924/>).
9. Vega, J. *et al.* Results of the JET real-time disruption predictor in the ITER-like wall campaigns. *Fusion Engineering and Design* **88**, 1228–1231 (2013).
 10. Rea, C. *et al.* Disruption prediction investigations using Machine Learning tools on DIII-D and Alcator C-Mod. *Plasma Phys. Control. Fusion* **60**, 084004 (2018).
 11. Zheng, W. *et al.* Hybrid neural network for density limit disruption prediction and avoidance on J-TEXT tokamak. *Nucl. Fusion* **58**, 056016 (2018).
 12. Yang, Z. *et al.* A disruption predictor based on a 1.5-dimensional convolutional neural network in HL-2A. *Nucl. Fusion* **60**, 016017 (2020).
 13. Cannas, B. *et al.* Overview of manifold learning techniques for the investigation of disruptions on JET. *Plasma Phys. Control. Fusion* **56**, 114005 (2014).
 14. Piccione, A., Berkery, J. W., Sabbagh, S. A. & Andreopoulos, Y. Physics-guided machine learning approaches to predict the ideal stability properties of fusion plasmas. *Nucl. Fusion* **60**, 046033 (2020).
 15. Rattá, G. A., Vega, J. & Murari, A. Improved feature selection based on genetic algorithms for real time disruption prediction on JET. *Fusion Engineering and Design* **87**, 1670–1678 (2012).
 16. Murari, A. *et al.* Investigating the Physics of Tokamak Global Stability with Interpretable Machine Learning Tools. *Applied Sciences* **10**, 6683 (2020).
 17. Vega, J. *et al.* Disruption prediction with artificial intelligence techniques in tokamak plasmas. *Nat. Phys.* **18**, 741–750 (2022).
 18. Yang, Z. *et al.* In-depth research on the interpretable disruption predictor in HL-2A. *Nucl. Fusion* **61**, 126042 (2021).
 19. Rea, C., Montes, K. J., Pau, A., Granetz, R. S. & Sauter, O. Progress Toward Interpretable Machine Learning-Based Disruption Predictors Across Tokamaks. *Fusion Science and Technology* **76**, 912–924 (2020).
 20. Chen, C. *et al.* This Looks Like That: Deep Learning for Interpretable Image Recognition. Preprint at <http://arxiv.org/abs/1806.10574> (2019).
 21. Rudin, C. Stop explaining black box machine learning models for high stakes decisions and use interpretable models instead. *Nat Mach Intell* **1**, 206–215 (2019).
 22. Davies, A. *et al.* Advancing mathematics by guiding human intuition with AI. *Nature* **600**, 70–74 (2021).
 23. Ribeiro, M. T., Singh, S. & Guestrin, C. ‘Why Should I Trust You?’: Explaining the Predictions of Any Classifier. Preprint at <http://arxiv.org/abs/1602.04938> (2016).
 24. Mothilal, R. K., Mahajan, D., Tan, C. & Sharma, A. Towards Unifying Feature Attribution and Counterfactual Explanations: Different Means to the Same End. in *Proceedings of the 2021 AAAI/ACM Conference on AI, Ethics, and Society* 652–663 (2021). doi:10.1145/3461702.3462597.
 25. Lundberg, S. & Lee, S.-I. A Unified Approach to Interpreting Model Predictions. Preprint at <http://arxiv.org/abs/1705.07874> (2017).
 26. Lundberg, S. M. *et al.* Explainable machine-learning predictions for the prevention of hypoxaemia during surgery. *Nat Biomed Eng* **2**, 749–760 (2018).
 27. Ke, G. *et al.* LightGBM: A Highly Efficient Gradient Boosting Decision Tree. 9.
 28. Zhong, Y. *et al.* Disruption prediction and model analysis using LightGBM on J-TEXT and HL-2A. *Plasma Phys. Control. Fusion* **63**, 075008 (2021).
 29. Tay, Y. *et al.* Scaling Laws vs Model Architectures: How does Inductive Bias Influence Scaling? Preprint at <http://arxiv.org/abs/2207.10551> (2022).
 30. Kates-Harbeck, J., Svyatkovskiy, A. & Tang, W. Predicting disruptive instabilities in controlled fusion plasmas through deep learning. *Nature* **568**, 526–531 (2019).
 31. Zhu, J. X. *et al.* Hybrid deep-learning architecture for general disruption prediction across multiple tokamaks. *Nucl. Fusion* **61**, 026007 (2021).
 32. Zhu, J. *et al.* Scenario adaptive disruption prediction study for next generation burning-plasma tokamaks. *Nucl. Fusion* **61**, 114005 (2021).
 33. Murari, A. *et al.* On the transfer of adaptive predictors between different devices for both mitigation and prevention of disruptions. *Nucl. Fusion* **60**, 056003 (2020).
 34. Vaswani, A. *et al.* Attention Is All You Need. Preprint at <http://arxiv.org/abs/1706.03762> (2017).
 35. White, R. B., Monticello, D. A. & Rosenbluth, M. N. Simulation of Large Magnetic Islands: A

- Possible Mechanism for a Major Tokamak Disruption. *Phys. Rev. Lett.* **39**, 1618–1621 (1977).
36. Du, X. D. *et al.* Direct measurements of internal structures of born-locked modes and the key role in triggering tokamak disruptions. *Physics of Plasmas* **26**, 042505 (2019).
 37. Carreras, B., Hicks, H. R., Holmes, J. A. & Waddell, B. V. Nonlinear coupling of tearing modes with selfconsistent resistivity evolution in tokamaks. 17 (2014).
 38. Pucella, G. *et al.* Onset of tearing modes in plasma termination on JET: the role of temperature hollowing and edge cooling. *Nucl. Fusion* **61**, 046020 (2021).
 39. Li, J., Ding, Y., Zhang, X., Xiao, Z. & Zhuang, G. Design of the high-resolution soft X-ray imaging system on the Joint Texas Experimental Tokamak. *Review of Scientific Instruments* **85**, 11E414 (2014).
 40. Zhang, X. L., Cheng, Z. F., Hou, S. Y., Zhuang, G. & Luo, J. Upgrade of absolute extreme ultraviolet diagnostic on J-TEXT. *Review of Scientific Instruments* **85**, 11E420 (2014).
 41. Greenwald, M. *et al.* A new look at density limits in tokamaks. *Nucl. Fusion* **28**, 2199–2207 (1988).
 42. Chen, J., Gao, L., Zhuang, G., Wang, Z. J. & Gentle, K. W. Design of far-infrared three-wave polarimeter-interferometer system for the J-TEXT tokamak. *Review of Scientific Instruments* **81**, 10D502 (2010).
 43. Han, D. *et al.* Magnetic diagnostics for magnetohydrodynamic instability research and the detection of locked modes in J-TEXT. *Plasma Sci. Technol.* **23**, 055104 (2021).
 44. Lundberg, S. M. *et al.* From local explanations to global understanding with explainable AI for trees. *Nat Mach Intell* **2**, 56–67 (2020).
 45. Friedman, J. H. Greedy function approximation: A gradient boosting machine. *Ann. Statist.* **29**, (2001).
 46. Rashmi, K. V. & Gilad-Bachrach, R. DART: Dropouts meet Multiple Additive Regression Trees. Preprint at <http://arxiv.org/abs/1505.01866> (2015).
 47. *The Shapley value: essays in honor of Lloyd S. Shapley.* (Cambridge University Press, 1988).
 48. Slack, D., Hilgard, S., Jia, E., Singh, S. & Lakkaraju, H. Fooling LIME and SHAP: Adversarial Attacks on Post hoc Explanation Methods. in *Proceedings of the AAAI/ACM Conference on AI, Ethics, and Society* 180–186 (ACM, 2020). doi:10.1145/3375627.3375830.
 49. Ding, Y. *et al.* Overview of the J-TEXT progress on RMP and disruption physics. *Plasma Sci. Technol.* **20**, 125101 (2018).
 50. Wang, N. *et al.* Advances in physics and applications of 3D magnetic perturbations on the J-TEXT tokamak. *Nucl. Fusion* **62**, 042016 (2022).
 51. Huang, M. *et al.* The operation region and MHD modes on the J-TEXT tokamak. *Plasma Phys. Control. Fusion* **58**, 125002 (2016).
 52. Shi, P. *et al.* Observation of the high-density front at the high-field-side in the J-TEXT tokamak. *Plasma Phys. Control. Fusion* **63**, 125010 (2021).
 53. Shi, P. *et al.* First time observation of local current shrinkage during the MARFE behavior on the J-TEXT tokamak. *Nucl. Fusion* **57**, 116052 (2017).
 54. Hu, Q. *et al.* Research on the effect of resonant magnetic perturbations on disruption limit in J-TEXT tokamak. *Plasma Phys. Control. Fusion* **58**, 025001 (2016).